Available online at www.sciencedirect.com
SCIENCE DIRECT®
International Journal of Heat and Mass Transfer 47 (2004) 4349–4363
International Journal of HEAT and MASS TRANSFER
www.elsevier.com/locate/ijhmt

Visualization of the subcooled flow boiling of R-134a in a vertical rectangular channel with an electrically heated wall

In Cheol Bang [a,*], Soon Heung Chang [a], Won-Pil Baek [b]

[a] Korea Advanced Institute of Science and Technology, 373-1 Guseong-dong, Yuseong-gu, Daejeon 305-701, Republic of Korea
[b] Korea Atomic Energy Research Institute, 150 Dukjin-dong, Yuseong-gu, Daejeon 305-353, Republic of Korea

Received 14 November 2003; received in revised form 15 April 2004

Abstract

A digital photographic study of subcooled flow boiling with R-134a was performed in a vertical rectangular channel heated from one side to observe near-wall structures. Primary attention was given to bubble formation and bubble coalescence in the bubble layer. The visualization made possible a detailed observation of the characteristic near-wall region, consisting of vapor remnants, an interleaved liquid layer, and coalesced adjacent bubbles. In particular, the visualization provided clearer insights about bubble coalescence behaviors during flow nucleate boiling. In addition, it is shown that the near-wall bubble layer of nucleate boiling beneath vapor clots is extinguished and, afterwards, the heated surface is locally covered by large vapor films, at CHF.

Keywords: R-134a; Near-wall region; Bubble coalescence; CHF; Visualization

1. Introduction

To enhance energy transfer efficiency, forced convective nucleate boiling, which is common in various heat transfer systems, is very effective in achieving a high heat flux with a small temperature difference between the heated surface and the cooling fluid. Forced convective nucleate boiling has a limitation, however: departure from nucleate boiling (DNB). This limitation is characterized by the highest heat transfer rate and the initiation of heat transfer surface damage. The damage is directly related to the physical burnout of the materials of the heat exchanger. However, the physical mechanism of this limitation has not been understood clearly. As visualization of the near-wall region at high heat flux and high mass flux is very difficult, the relevant detailed information is not available. A review of previous research concerning high heat fluxes near and at DNB reveals that the following phenomena have been observed in relation to the mechanism triggering DNB:

(a) a bubble crowding phenomenon,
(b) a blanketing phenomenon, by a vapor clot or a vapor blanket,
(c) a wavelike succession of vapor clots phenomenon.

In the low pressure tests of water by Gunther [1] and Kirby et al. [2], an increase of bubble population and the formation of vapor clots were commonly observed with an increase of heat flux. In the high pressure and subcooling tests of water by Celata et al. [3], it was observed that the vapor blanket rooted to the nucleation site on the heated surface. In high pressure tests of Freon-113 by Tong et al. [4] and Mattson et al. [5], a bubble crowding phenomenon, involving the piling up of bubbles, and the formation of a clump by the agglomerations of bubbles were mainly observed. Recently, in the

* Corresponding author. Tel.: +82-42-869-3856; fax: +82-42-869-3810.
E-mail addresses: musoyou@kaist.ac.kr (I.C. Bang), shchang@kaist.ac.kr (S.H. Chang), wpbaek@kaeri.re.kr (W.-P. Baek).

0017-9310/$ - see front matter © 2004 Elsevier Ltd. All rights reserved.
doi:10.1016/j.ijheatmasstransfer.2004.04.030

Nomenclature

BL	bubble layer
NBL	near-wall bubble layer
BH	bubble height: the thickness in channel width of the maximum bubble
BL	bubble length: the length in flow direction of the maximum bubble
D	diameter, m
L	length, m
G	mass flux, $kg\times m^{-2}\times s^{-1}$
p	pressure, bar
q	heat flux, $kW\times m^{-2}$
T	temperature, °C
x	thermodynamic quality

Subscripts

e	exit
in	inlet
sat	saturation
w	wall (measured temperature)

FC-87 and FC-72 tests of Galloway and Mudawar [6] and Sturgis and Mudawar [7], a vapor wave pattern was newly observed near and at CHF. This vapor wave pattern seems to be formed by vivid vapor coalescences.

In spite of the aforementioned observations, there is still no complete understanding of the mechanisms that lead to the triggering of DNB. Various hypothetical mechanisms have been put forth as the primary causes of DNB, but no theoretical models with good prediction performances have been found to be closely linked to the visualization results. Weisman and Pei [8] postulated that CHF occurs when the volume fraction of steam in the bubble layer slightly exceeded a critical void fraction. Larson and Tong [9] developed an analytical model for a void fraction distribution in subcooled flow boiling, assuming a three-layer structure. Lee and Mudawar [10] postulated that CHF occurs because of the Helmholtz instability, if the heat flux is sufficient for liquid sublayer dryout below the vapor blanket. Chun et al. [11] also proposed a CHF model, based on the concept of superheated liquid layer depletion. The visualization results of previous research depended on macroscopic flow patterns; however, due to the complex phenomena involved with boiling, macroscopic observations can

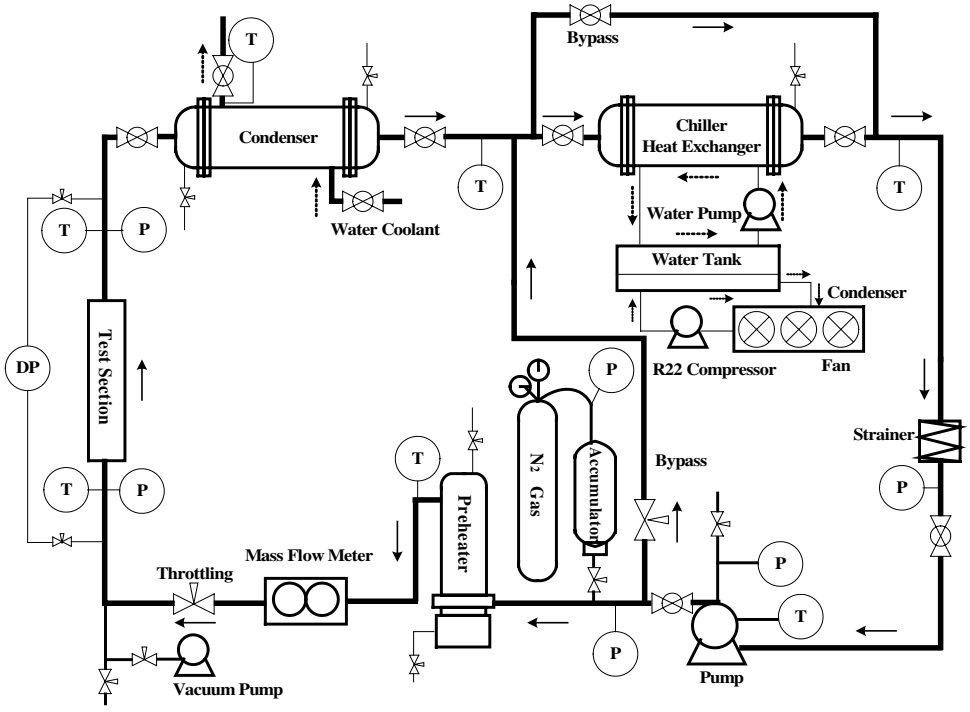

Fig. 1. Schematic diagram of the experimental system.

provide no further breakthrough about a possible mechanism for DNB. The hypotheses of many theoretical models are unclear. Therefore, more effort is needed to visualize a near-wall region in detail. The recent visualization results of Chang et al. [12], reported a characteristic boiling flow structure of the superheated liquid layer with small bubbles attached to the heated wall, a flowing bubble layer, including large coalesced bubbles, and a liquid core. The objective of this study is to improve on previously reported information by means of a new digital photographic study and to provide a qualitative description for unclear aspects of the near-wall region phenomena. As a working fluid, R-134a was selected to replace other refrigerants banned due to their destruction of the ozone layer and for the high pressure–high temperature simulation of a water-cooled system. Image technology has advanced considerably in recent decades, especially with the rise of optical photographic technology and digital technology. This enables researchers to overcome certain difficulties of the visualization study of complex boiling phenomena. This paper reports on the investigation of the subcooled flow boiling of R-134a, using digital imaging technology.

2. Experimental method

2.1. Experimental loop

The experiment on the subcooled flow boiling of R-134a was performed in a range of 0–2000 kg/m^{2}s of mass fluxes and 9–25 °C of inlet subcooling, under 7 and 14.5 bars of pressure, respectively. The apparatus of the present experiment is shown in Fig. 1. The R-134a experimental loop consists of the following components: a test section for visualization, a mass flow meter, a pre-heater for inlet subcooling control, an accumulator for pressure control, a non-seal canned pump for stable mass supply, a condenser with phase change, and a chiller, or chilling system, with R-22 and water–propylene glycol. The chiller used contains a heat exchanger for R-134a cooling, with water–propylene glycol flow via a water pump cooled in a bath with an R22 refrigeration system. The loop is filled with R-134a in the vacuum condition. A data acquisition system is used and electric power to heat the boiling surface of the test section is supplied by a DC power supply, with the maximum capacity of 4.375 kW (5 V, 875A).

2.2. Test section

A vertical rectangular channel heated from one side was used, as shown in Fig. 2. The apparatus consists of a channel body, an inserter containing a heating plate, and a flow developing body. The developing body in the lower part has an entrance length more than 40 times the channel hydraulic diameter, to provide the channel with a fully developed turbulent flow. The channel body is made of aluminum alloy and provides a flow channel of 8 mm (width, including the heated surface)×5 mm (height, with window) and polycarbonate windows for the visualization of the front and the side. The inserter was made of Bakelite, as an insulator, and a heating plate of Inconel 600, which measured 4 mm (width)× 100 mm (length)×1.9 mm (thickness). The plate was heated by DC power that was supplied through copper electrodes connected to the plate at both sides. The

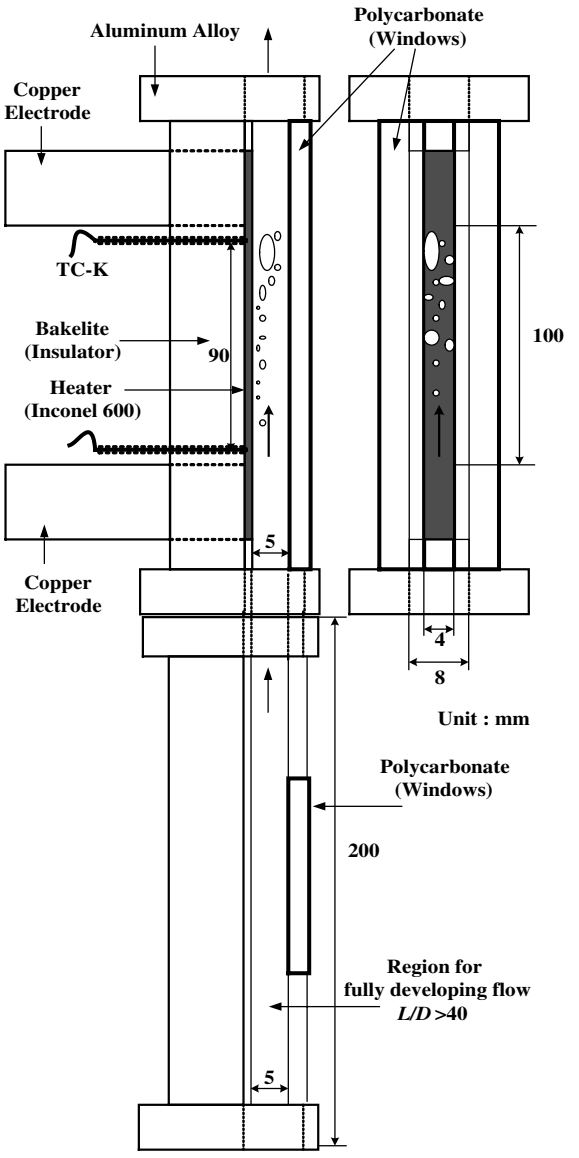

Fig. 2. Schematic diagram of the test section for flow boiling visualization.

Bakelite insulator assured sufficient insulation, allowing only a negligible heat loss to the surrounding air. To measure the heater surface temperature, two thermocouples of type K were embedded in the heating plate of Inconel 600, at the positions of 1 and 9 mm from the leading edge (i.e., the top of the heated section) and 0.4 mm in depth from the heated surface. The indirect measurement of temperature on the heated surface is corrected by using a heat diffusion equation [12].

2.3. Digital photographic method for visualization

In this study, a flow boiling structure of the channel was visualized with an advanced digital photographic technique. In previous studies that used analog cameras, a large amount of time was required to fix the intensity of light properly and to develop film. A digital camera was used in our study to improve efficiency over previous methods. The digital camera used has a flash-synchronized shutter speed of 1/500 s, a total 2.74 million pixels CCD (record pixels 2000×1312 which is used really), and uses flash memory instead of analog film. The optical lenses can be interchanged to increase magnification. The optical visualization conditions can be arranged so that the digital system captures the intensity and the surrounding conditions. Therefore, only a short luminescence time is needed to acquire a clear still image. While the shutter was open (camera B shutter) in the experiment, the high-speed flash with short duration time of 1/8700 s was emitted into the flow channel. As a light source, two flashes were used in a single and double flash method that requires a synchronizing device. Continuous photos were taken, with a time interval of 0.22 sec. Fig. 3 shows a schematic of the digital photographic system used. To magnify the phenomena shown in the flow channel, a 105 mm Macro lens was used, along with three extension tubes of 14, 21, and 31 mm, for close-ups. While focusing, a Halogen lamp of 2000 W was used as the auxiliary light source. After capturing an image of a fast moving bubble, image processing was performed, using commercial image processing software, to correct the brightness and contrast of the images, and to make measurements of the bubble dimension parameters. The digital camera provided a spatial resolution of $\sim$10 μm per pixel to the images of the visual test.

2.4. Uncertainty analysis

The uncertainties of the measurement parameters are analyzed by the error propagation method [17]. The uncertainties of the applied heat flux and mass flux were less than ±1.0% and ±1.3% respectively. Uncertainties for the pressure and temperature measurements are ±9 kPa and ±0.5 °C, respectively. The heater surface temperature has an uncertainty of approximately ±2 °C at a heat flux of 507 kW/m^2, depending on the heat flux and the embedding distance. The bubble size and bubble layer thickness from the image processing of the original images have uncertainties of approximately 3% and 4%, respectively.

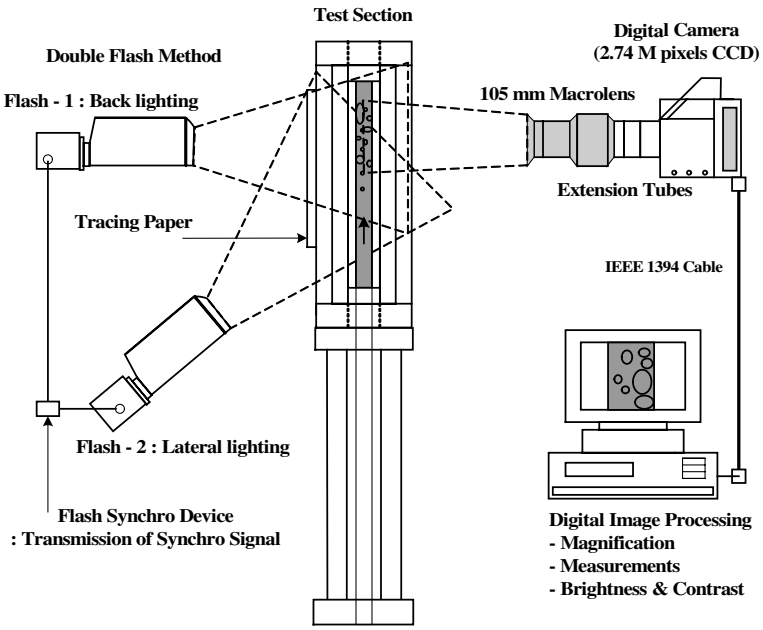

Fig. 3. Schematic diagram of the digital photographic system.

3. Results and discussion

The visualization was achieved at the front and the sides of the flow channel, and an indirect measurement of the heated surface temperature was performed to ascertain boiling curves and, consequently, to represent the main range of visual test conditions. The overall observation of the flow channel was performed to observe the macroscopic flow pattern, including a bubble layer and a bubble coalescence phenomena in the bubble layer with the heated surface. A partial observation of the flow channel was performed to obtain largely magnified images of the near-wall region, with a large spatial resolution of up to several tens of microns.

3.1. Boiling curves and visualization conditions

Fig. 4 shows the boiling curves in the present visualization experiment. The temperatures measured from the heated wall represent the typical relation of heat flux vs. wall temperature between a single-phase region and two-phase region. As the mass flux increases, the wall temperature decreases at same heat flux in the single-phase region, but there is no change in the two-phase region. Visualization was performed mainly in the two-phase region, from a low heat flux (5–10% of CHF) of the ONB (Onset of Nucleating Boiling) with discrete bubbles, to a high heat flux (70–80% of CHF) with large vapor clots, by a violent coalescing behavior of those bubbles, or CHF. Table 1 shows the experimental conditions of the present study. The quality x_e is the thermodynamic equilibrium quality averaged for the cross section near the channel exit, which is calculated based on the inlet mass flux, the inlet enthalpy, and the heat input.

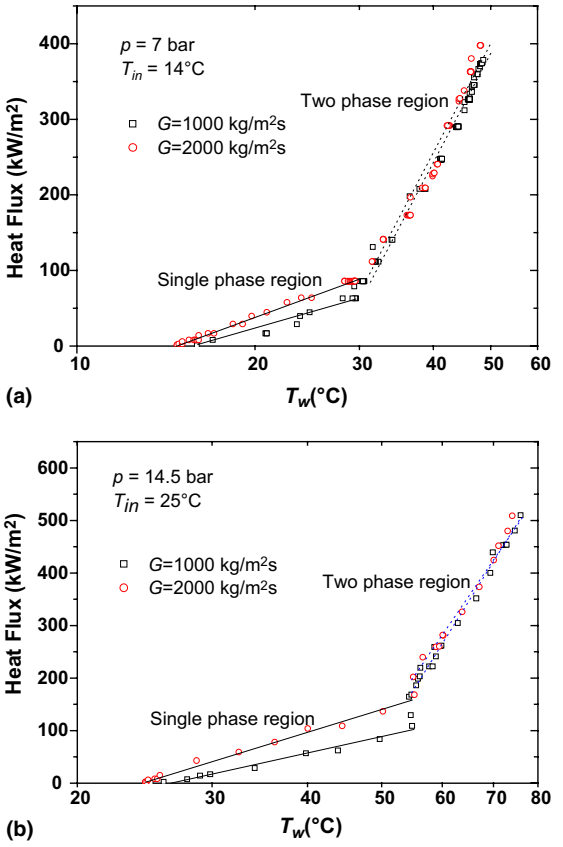

Fig. 4. Representative boiling curve in the present visualization experiment.

3.2. Macroscopic flow pattern

Fig. 5(a) and (b) show the general bubble behavior on the heated surface: there are vertically flowing bubbles at both a zero liquid flow rate and a low flow rate. These figures illustrate the development of the bubble layer along the heated surface relative to the increase of heat flux. Bubbles begin to form actively on the surface with the increase of heat flux and later coalesce vividly with each other in the bubble layer. Finally, the agglomerations form the slug bubbles or large vapor clot at bulk flow. The overall flow pattern may reveal a similar trend, or apparently reliable characteristics, between R-134a as a modeling fluid and water as an original fluid.

3.2.1. From discrete bubble formation to coalesced bubble formation

Front and lateral observation photos were taken of the partially heated surface and the local flow channel near the exit, with the change of heat and mass fluxes in

Table 1
Test conditions

p	T_i	x_e	G	q	Visualization
7 (T_{sat} ~ 26.86 °C)	9, 14, 19	−0.049 to +0.059	0, 190	~411	Overall lateral observation
		−0.137 to −0.025	1000	~875	Local front and lateral observation
		−0.138 to −0.037	2000	~955	Local front and lateral observation
14.5 (T_{sat} ~ 53.9 °C)	25	−0.245 to −0.207	1000	~830	Local lateral observation
		−0.246 to −0.233	2000	~873	Local lateral observation

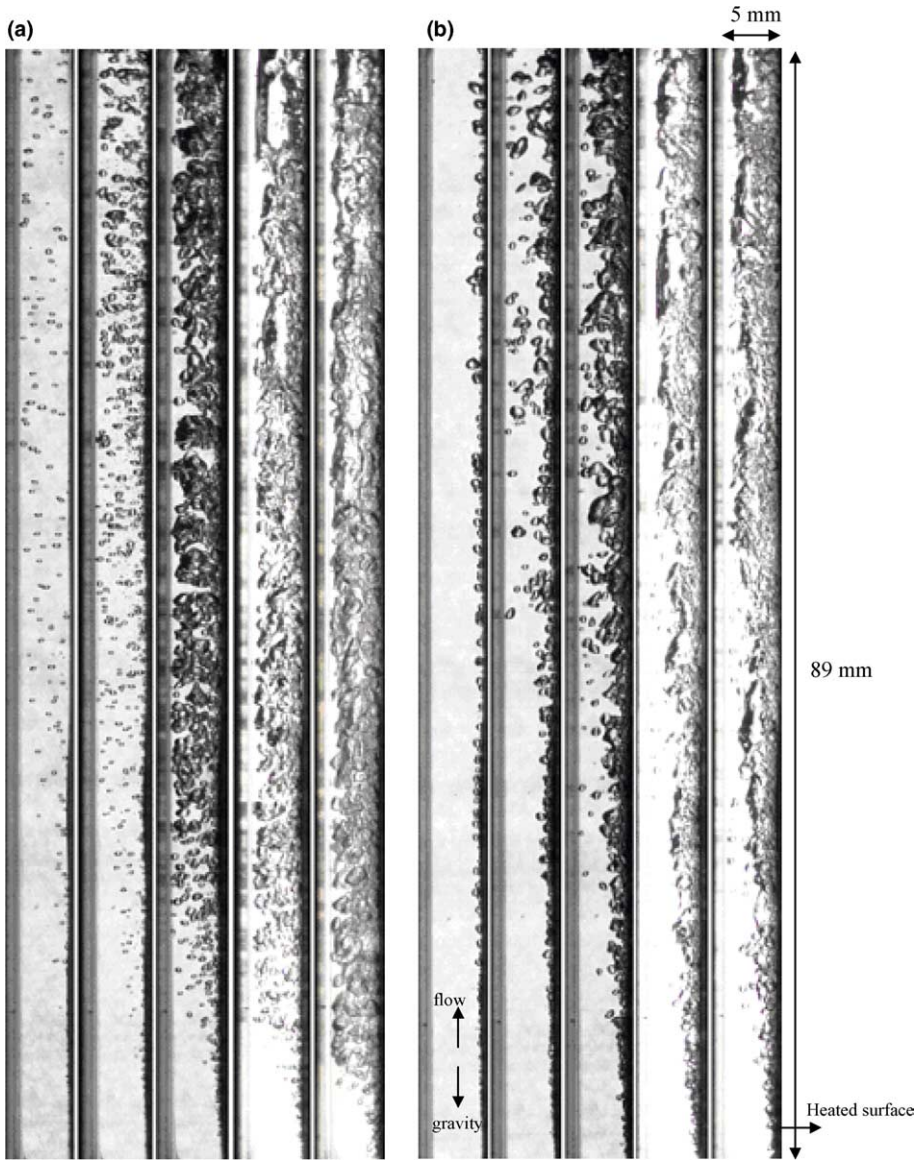

Fig. 5. Overall flow pattern. (a) Pool boiling, lateral observation: $p = 7$, $G = 0$, q (kW/m^2) = 7.6, 17, 46, 90, 163. (b) Low flow boiling, lateral observation: $p = 7$, $G = 190$, q (kW/m^2) = 47, 119, 216, 360, 411 $x_e = -0.049, -0.028, -0.001, +0.044, +0.059$.

Fig. 6. In a range of low heat flux, as shown in the figures, a single-phase heat transfer was achieved first; then, in a heat flux over nucleation condition, discrete bubbles were observed on the heated surface. Bubbles repeatedly grow and collapse, but with the further increase of heat flux, some bubbles began to break away and move with the bulk flow and along the flow channel. With the increase of heat flux, a further increase of bubble separation and active nucleation sites causes the vivid bubble coalescences of over 30–40% of CHF, as shown in the photos. As a result of the bubbles coalescence, large bubbles formed; then, the large coalesced bubbles developed larger sized vapor clots, with more activation of nucleation sites of over 70–80% of CHF. These vapor clots were observed periodically along the heated surface. The cause of these vapor clot formations is the activation of nucleation sites and bubble departure frequency. The average size of the bubbles or the coalesced bubbles, before separation, decreases with an increase of the mass flux. Discrete bubbles have an elliptical shape when viewed from the side and a round shape when viewed from the front.

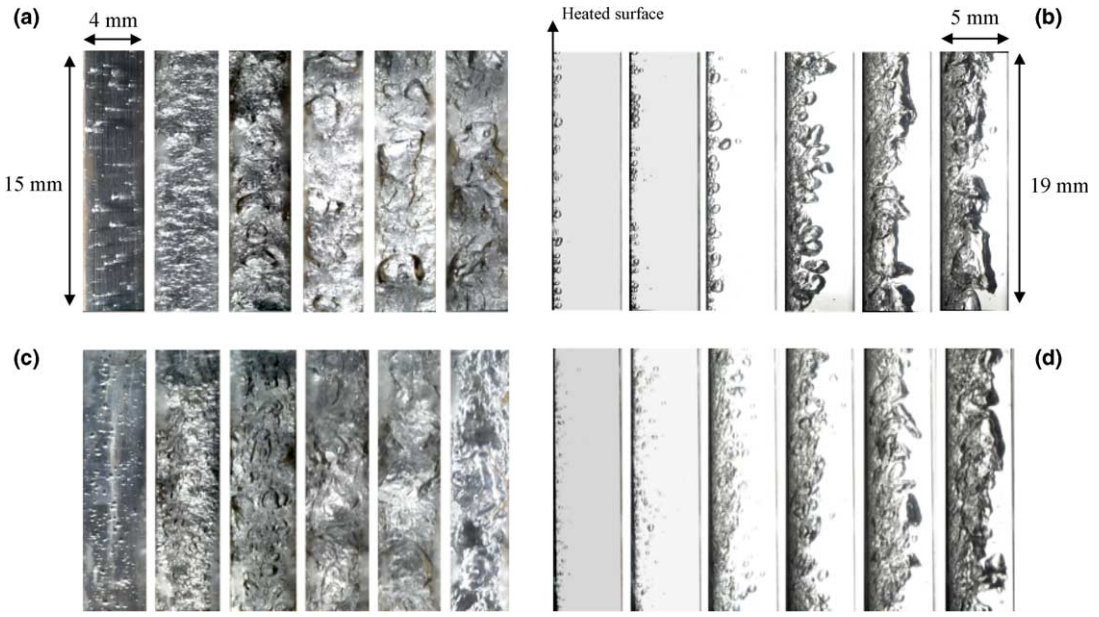

Fig. 6. Bubble behaviors from discrete bubble regime to coalesced bubble regime. (a) Front observation ($p = 7$, $G = 1000$): q (kW/m^2) = 53, 142, 243, 303, 366, 477; % of CHF = 6.1, 16.2, 27.8, 34.6, 41.8, 54.5; $x_e = -0.061, -0.055, -0.050, -0.046, -0.043, -0.036$. (b) Lateral observation ($p = 7$, $G = 1000$): q (kW/m^2) = 82, 82, 120, 215, 474, 670; % of CHF = 9.4, 9.4, 13.7,24.6, 54.2, 76.6; $x_e = -0.059, -0.059, -0.057, -0.051, -0.037, -0.025$. (c) Front observation ($p = 7$, $G = 1000$): q (kW/m^2) = 80, 136, 295, 860, 899, 941 (CHF); % of CHF = 8.5, 14.5, 31.4, 91.4, 95.5, 100; $x_e = -0.061, -0.060, -0.055, -0.039, -0.038, -0.037$. (d) Lateral observation ($p = 7$, $G = 1000$): q (kW/m^2) = 102, 120, 313, 362, 530, 941; % of CHF = 10.8, 12.8, 33.3, 38.5, 56.3, 100; $x_e = -0.061, -0.060, -0.055, -0.053, -0.048, -0.037$.

3.2.2. Two regions of a bubble layer

As the heat flux increases, discrete bubbles form and then begin to coalesce with one another. This observation has been described as a ''bubble layer''. Through the present detailed observations, the bubble layer at a sufficiently high heat flux (30–40% of CHF) can be divided into two regions: a near-wall bubble layer and a large coalesced bubble layer.

The near-wall bubble layer consisting of small bubbles and interleaved liquid occupies areas under large vapor clots. This layer is the source of the vapor clots. The coalescence phenomena that form the large vapor clots are similar to those of boiling water [1,2,12]. The coalescence of bubbles occurs in two ways: (1) by an increased coalescing among discrete bubbles at neighboring nucleation sites and (2) by the merging of growing bubbles at nucleation sites into larger flowing bubbles. During the coalescence process, the large vapor clots have growth and size limitations, due to Helmholtz instability, which is related to waves observed on the surface of the vapor clots. This observation is well known and is reported in the research of Galloway and Mudawar [6]. The two regions of near-wall bubbles and large vapor clots are also shown clearly in Fig. 7. Therefore, the flow structure of boiling, at a sufficiently high heat flux, is characterized as follows:

1. a near-wall bubble layer with small bubbles,
2. a flowing bubble layer with large coalesced bubbles, and
3. a liquid core.

This three-layer structure is very closely linked to both the occurrence of CHF in the experiment and the boiling water flow structure of Chang et al. [12], comprising a superheated liquid layer, with very small bubbles attached on the heated surface, a flowing bubble layer containing vapor clots, and a liquid core.

3.2.3. Effect of flow parameters on macroscopic flow pattern

Generally, subcooled flow boiling is characterized by the formation of bubbles at the heated surface. The formation of bubbles is altered mainly by flow parameters, such as mass flux, subcooling, and pressure. Fig. 7 shows the effects of these parameters. Fig. 8 shows the statistical average values, with each confidence interval, of the measured dimensions of bubble layers, near-wall bubble layers, and the height in the channel width and the length in the flow direction of bubbles having the maximum size in the images. As the mass flux increases, the heat transfer becomes more efficient, and wall superheat decreases, causing a decrease in the bubble

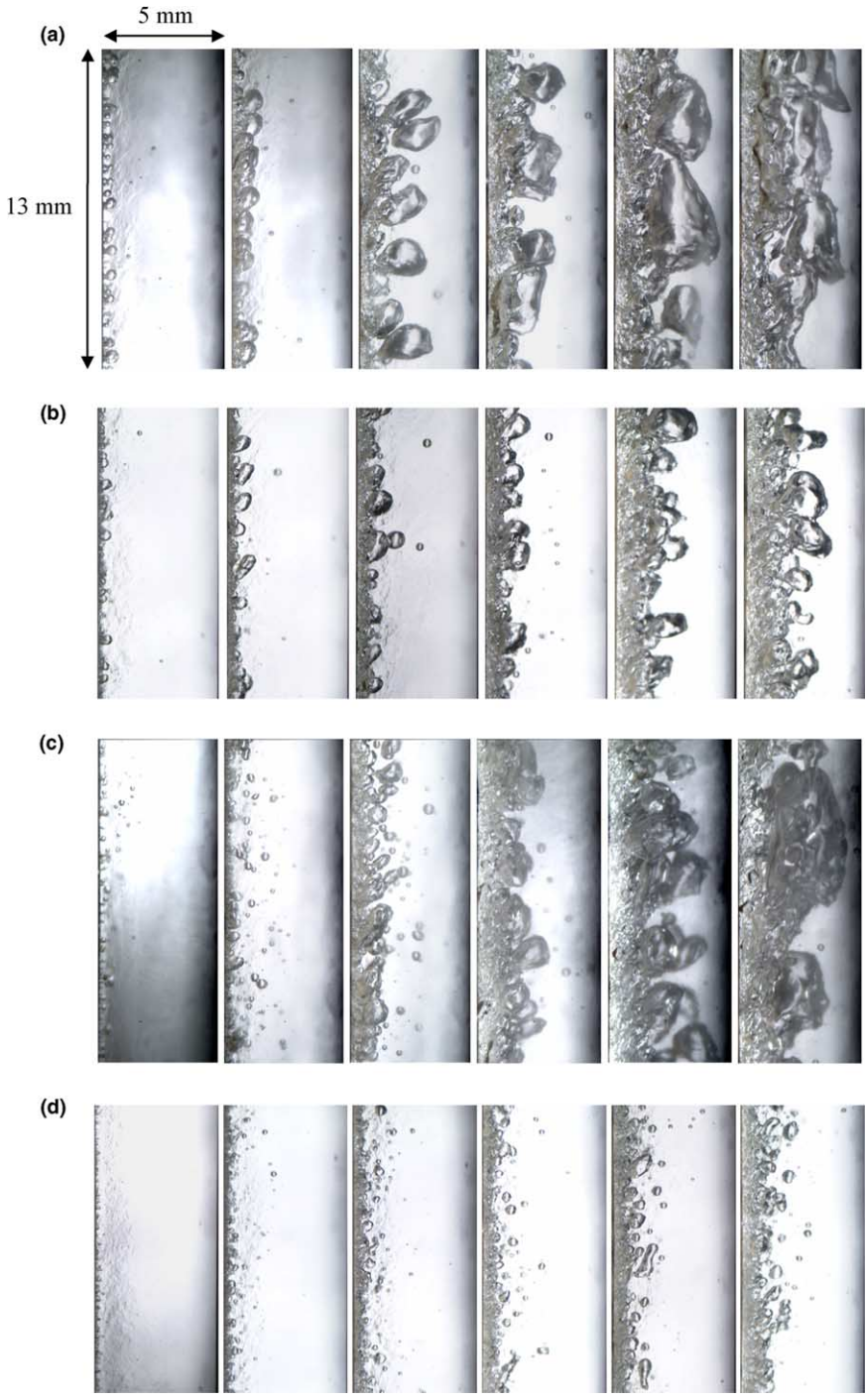

Fig. 7. Effect of flow parameters on boiling phenomena. (a) Lateral observation at lower pressure: $p = 7$, $G = 1000$; q (kW/m^2) = 84, 169, 330, 428, 571, 660; $x_e = -0.137, -0.132, -0.123, -0.118, -0.109, -0.104$. (b) Lateral observation at higher pressure: $p = 14.5$, $G = 1000$; q (kW/m^2) = 260, 350, 400, 507, 758, 830; $x_e = -0.245, -0.239, -0.236, -0.228, -0.212, -0.207$. (c) Lateral observation at lower pressure: $p = 7$, $G = 2000$; q (kW/m^2) = 137, 202, 376, 538, 727, 955; $x_e = -0.138, -0.136, -0.131, -0.127, -0.121, -0.115$. (d) Lateral observation at higher pressure: $p = 14.5$, $G = 2000$; q (kW/m^2) = 478, 567, 660, 725, 792, 873; $x_e = -0.246, -0.243, -0.240, -0.238, -0.236, -0.233$.

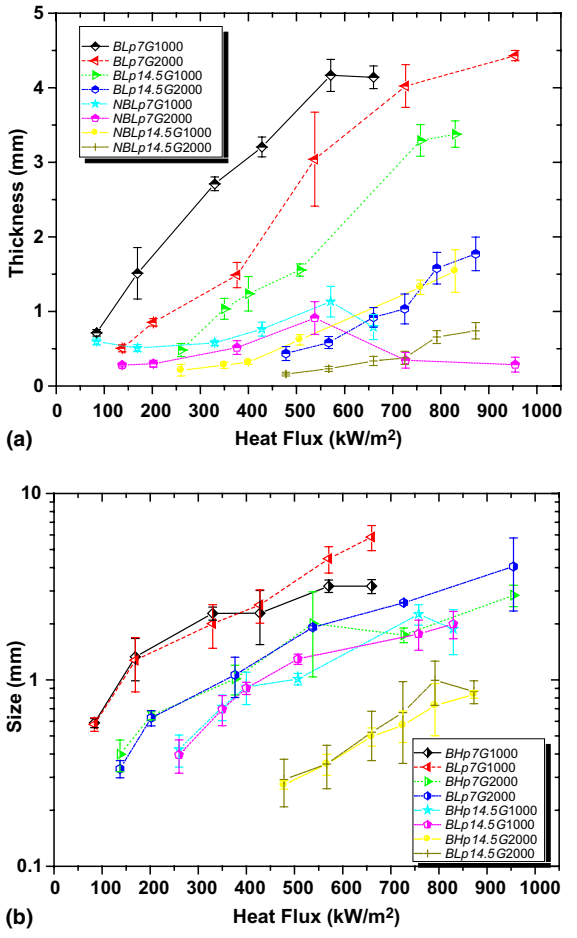

Fig. 8. Measurement of bubble parameters: (a) bubble layer thickness and (b) bubble size.

population. When the size of the bubbles decreases, the size of the coalesced bubbles also decreases. A faster flow rate causes more bubbles to separate from the wall, so that more flowing bubbles are observed in the bulk flow. However, there is no change in the macroscopic flow pattern of a bubble layer with the two regions of a near-wall bubble layer and large bubbles. This phenomenon is illustrated in Fig. 7(a) vs. (c) and Fig. 7(b) vs. (d).

Fig. 7(a) vs. (b) and Fig. 7(c) vs. (d) show the effects of pressure and subcooling. Higher pressure makes the size of the bubbles smaller, while higher subcooling causes faster bubble collapse, in the cycle of bubble growth and collapse. Therefore, in higher pressure, the size of discrete bubbles becomes smaller and the thickness of a bubble layer becomes thinner. As a mass flux effect, there is no large change in the macroscopic flow pattern of a bubble layer with the two regions of near-wall bubble layer and large bubbles. Only the size of the vapor clots or the overall dimension of the flow pattern decreases significantly.

3.3. Critical heat flux mechanism

The main objective of this study is to understand the physical mechanism leading to critical heat flux, through the detailed observation of the near-wall region. The appearance of vapor clots and bubble crowding phenomena occur near CHF, and vapor film appears on the heated surface at CHF. However, debate ensues among various researchers as to how the vapor clot and/or bubble crowding lead to transform the near-wall nucleating boiling region into vapor film region. The phenomenon of discrete bubble formation to vapor film formation at CHF has been illustrated in Fig. 6. Fig. 9 illustrates the successive observations of the CHF condition of the figure. The apparent flow pattern has a wavy boundary layer between the bubble layer and the liquid core, as shown in both the front and lateral views. Interactions between the near-wall bubble layer and the vapor clots, just before CHF, create a local dry area; then, a larger vapor film forms on the heated surface, as shown in Fig. 9(a). As a result, the near-wall bubble layer beneath the large vapor clots is removed.

Identifying the causal sequence leading to CHF is necessary to clearly describe the mechanism triggering CHF. Fig. 9(b) shows a series of photos used for this investigation. The first three photos show the successive events leading to CHF, or dryout, of the near-wall bubble layer. The other six photos show the successive events of the rewetting of the heated surface, after shutting the power off. The power supply of this experiment has an automatic power-off function for abrupt temperature increases of over ~50 °C, which are caused by the occurrence of CHF. The successive events triggering CHF are described as follows:

1. A near-wall bubble layer, with violent boiling beneath vapor clots, is observed approaching the exit.
2. The near-wall bubble layer is blanketed from the surrounding liquid flow by a passing vapor clot.
3. The near-wall bubble layer is transformed into a vapor film layer, due to instant evaporation or "dryout."
4. After the power is shut off, the vapor film, still remaining on the region of the near-wall layer beneath a passing vapor clot, causes blanketing near the exit.
5. After a short time, or if the wall temperature decreases to than Leidenfrost temperature, this vapor film is retransformed to the near-wall boiling region.

CHF is distinguished by the disappearance of the near-wall boiling region and the reappearance of the near-wall boiling region after the power is shut off. The present study concludes that CHF is characterized by the dryout of the near-wall bubble layer, with violent boiling below vapor clots, that is observed close to the

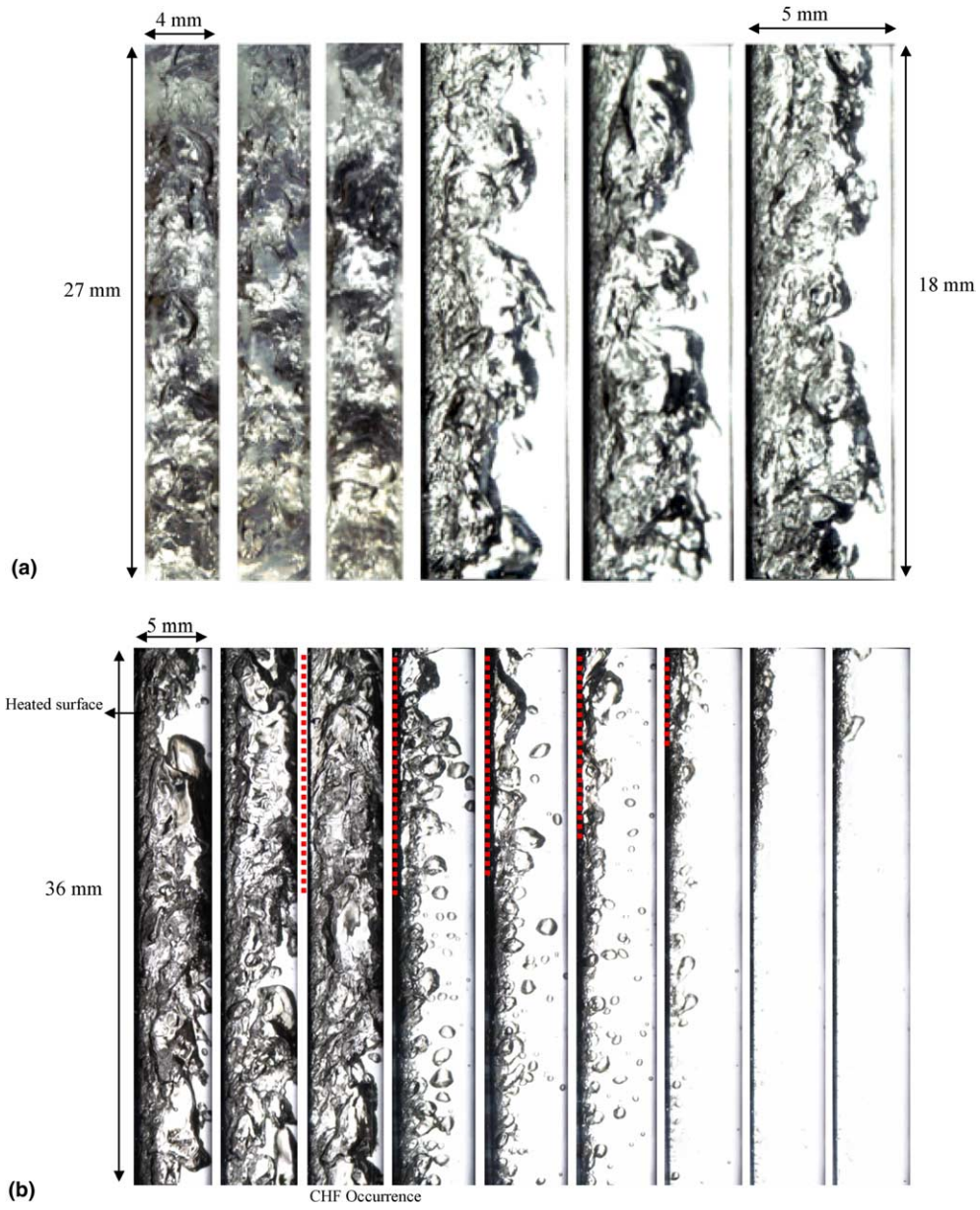

Fig. 9. Successive observations of the CHF condition. (a) Flow phenomena at CHF: front observation (3 photos), lateral observation (3 photos): $p = 7$, $G = 2000$, CHF (kW/m^2) = 941, $x_e = -0.037$. (b) Flow phenomena at CHF and after power-off. Lateral observation (vapor film: dot lines): $p = 7$, $G = 1000$, CHF (kW/m^2) = 875, $x_e = -0.092$ (3 photos), after power-off (6 photos).

exit, and by said layer being blanketed from the surrounding liquid flow by a passing vapor clot.

3.4. Microscopic observations of near-wall region

Through the present visualization experiment, it is observed that the near-wall bubble layer begins to develop with the onset of nucleate boiling (ONB) is removed with the occurrence of the CHF. It is possible that the existence of this layer plays an important role in the macroscopic mechanism of CHF. However, it is necessary to observe the formation and the structure of the near-wall bubble layer microscopically in order to acquire detailed information. This section of the paper reports on the microstructure-level triggers leading to CHF.

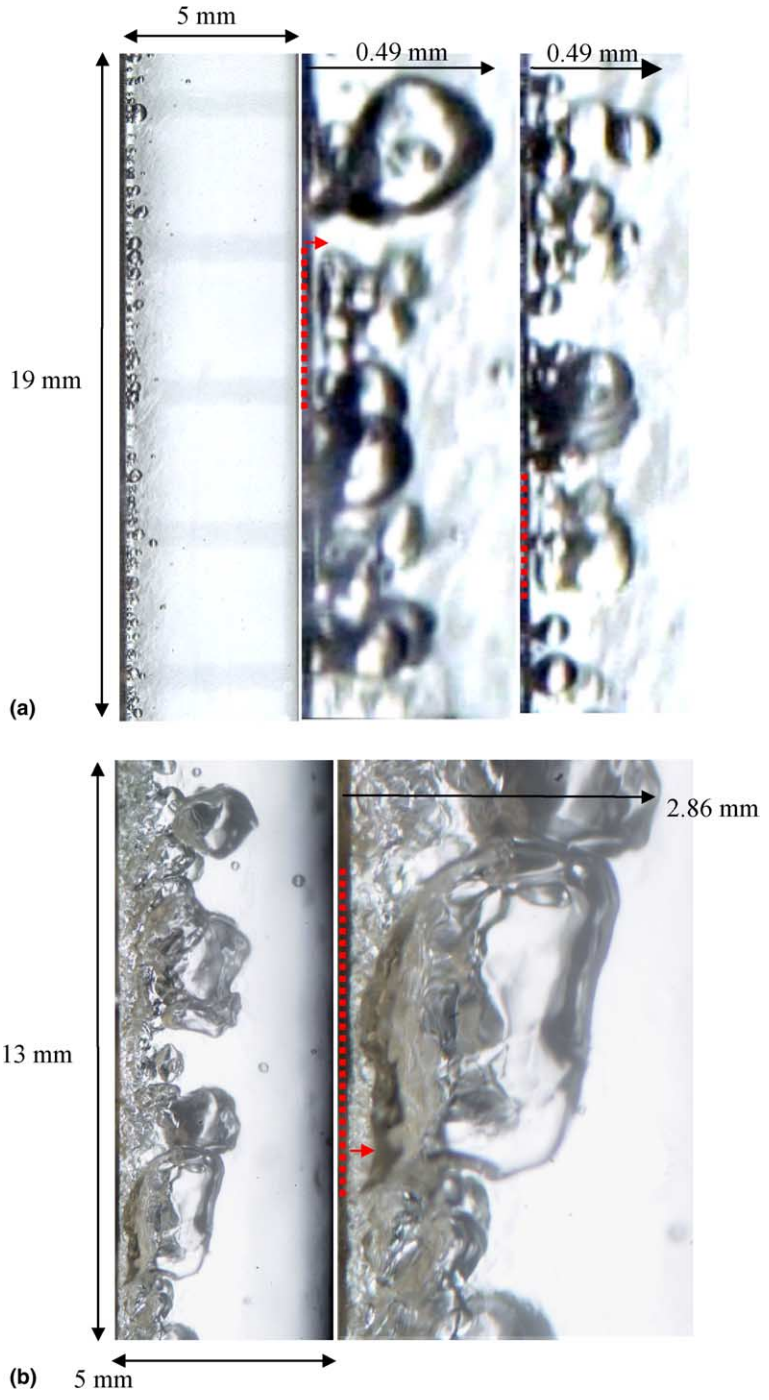

Fig. 10. Local liquid layer under coalesced bubbles or vapor clot. (a) Lateral observation: ~0.05 mm thickness liquid layer (small arrow); $p = 7$, $G = 1000$, q (kW/m^2) = 82 (9.4 % of CHF), $x_e = -0.059$. Partially magnified two photos on the right. (b) Lateral observation: ~0.2 mm thickness liquid layer (small arrow); $p = 7$, $G = 1000$, q (kW/m^2) = 428, $x_e = -0.118$. Partially magnified one photo on the right.

3.4.1. Liquid layer below coalesced bubbles

Fig. 10(a) shows the local liquid layer beneath coalesced bubbles, and Fig. 10(b) shows that a local liquid layer beneath a vapor clot can exist. The layer is also shown clearly in the boiling water research of Chang et al. [12]. That study considered the layer as a liquid

sublayer, which is assumed in many CHF models, such as Lee and Mudawar [10], Katto [13], and Celata [3]. Now, it is clear that the layer is blanketed from surrounding liquid, superheated, and not dried out at the low heat flux.

3.4.2. Vapor remnant and bubble neck

A bubble neck forms between the heated surface and the near-wall liquid region. As a bubble detaches from the surface, it divides into two vapor parts: the small vapor part stuck to the heated surface is the vapor remnant [14]; the other large vapor part is a detached bubble in a liquid flow. The vapor remnant is occasionally called a "dry spot" beneath a bubble, in the case of low heat flux [15]. Clear microscopic observations of the vapor remnant, bubble growth, and bubble detachment are shown in Figs. 11 and 12. This vapor remnant is observed not only beneath a single discrete bubble, but also beneath a large bubble, which is formed by the agglomeration of discrete bubbles. It can be called a "large dry spot" or a "dry patch" on the wall in low heat flux. Naturally this can be rewetted and is partially or completely condensed by liquid flow, with the separation of the bubbles.

3.4.3. Bubble group consisting of vapor remnants, a liquid layer, and bubbles

Our microscopic observations lead us to conclude that the near-wall region is characterized by a bubble group consisting of vapor remnants, an interleaved liquid layer, and bubbles, as shown in Fig. 11(c). As the heat flux increases, many bubble groups are formed because of nucleation site distribution and these groups constitute the near-wall bubble layer. Coalesced bubbles have a base with growing bubbles, vapor remnants, and a liquid layer. To increase the heat flux, the liquid inside a bubble group will be gradually dried, and then fully dried out, by an interaction such as the blanketing of a large vapor clot.

The second photo in Fig. 11(b) shows very tiny bubbles (of about 80 μm) on the heated wall, which may be considered as the initial nucleation. The microstruc-

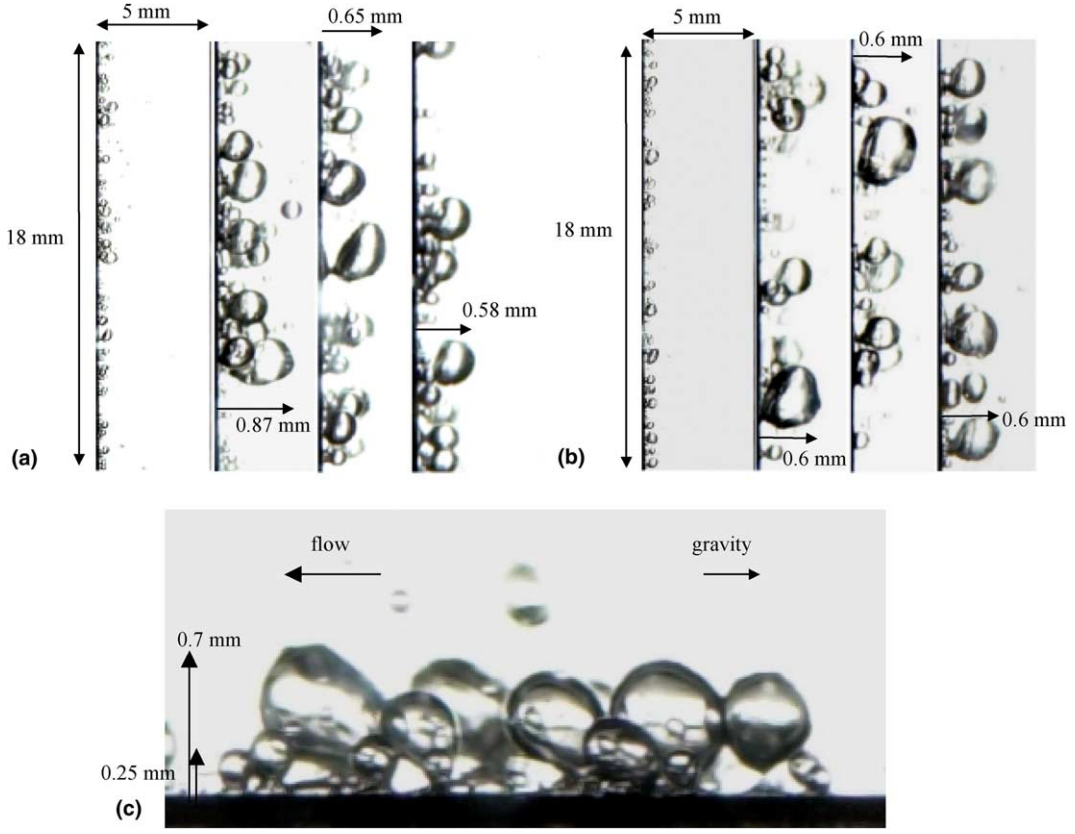

Fig. 11. Structure of bubbles on the wall. (a) Lateral observation: $p = 7$, $G = 1000$, $q = 82$ kW/m^2 (9.4% of CHF), $x_e = -0.059$. Partially magnified three photos on the right. (b) Lateral observation: $p = 7$, $G = 1000$, $q = 82$ kW/m^2 (9.4 % of CHF), $x_e = -0.059$. Partially magnified three photos on the right. (c) Bubble group of bubbles, vapor remnants and interleaved liquid layer: $p = 7$, $G = 1000$, $q = 82$ kW/m^2 (9.4 % of CHF), $x_e = -0.059$.

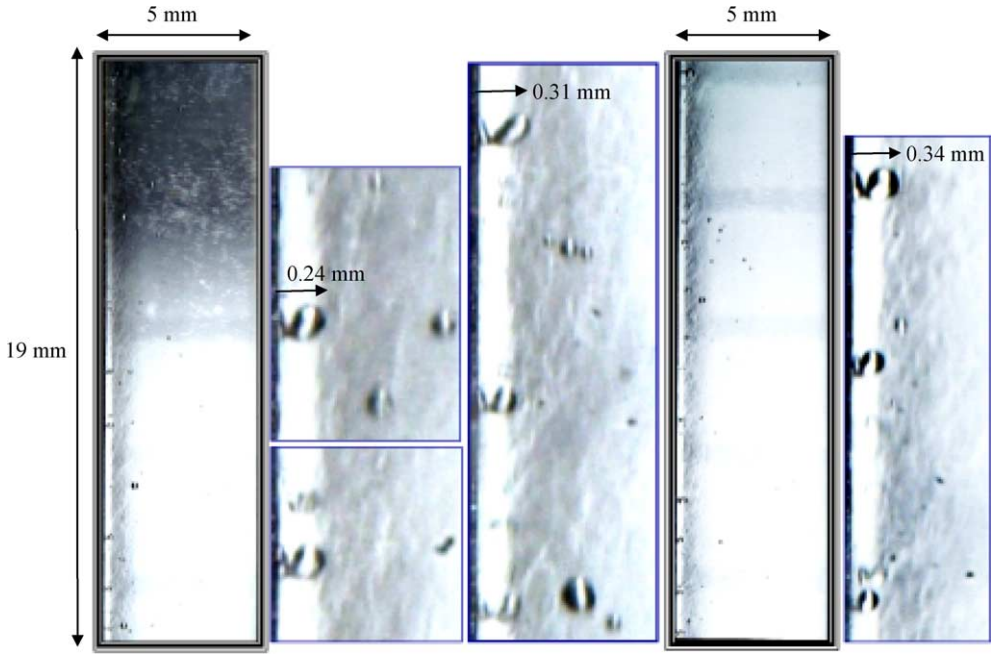

Fig. 12. Bubbles and vapor remnants on the wall. Lateral observation: $p = 7$, $G = 2000$, $q = 82$ kW/m^2 (8.7 % of CHF), $x_e = -0.061$. Partially magnified photos.

ture in this study was clearly observed with better resolution than those of previous studies.

3.5. Coalescence phenomenon

In this paper, we report that coalescence or agglomeration generally plays an essential role in causing the noticeable void fraction in a channel, leading to large vapor clot formation, or small dry area formation, by vapor remnants on the heated surface. The visualization results of the present work provide qualitative descriptions for coalescence behavior. For a two-phase flow, Bonjour et al. [16] summarized that there are three types of coalescence, distinguished as follows: (1) Coalescence far away from the heated wall, (2) Coalescence between consecutive bubbles near the wall and (3) Coalescence between adjacent bubbles near the wall.

As to the effects of the coalescences, it is generally known that coalescence between adjacent bubbles leads to vaporization of liquid beneath discrete bubbles by latent heat transfer, until a coalesced bubble separates from the wall. Therefore, it is thought that if many bubbles form on neighboring nucleation sites, as the aforementioned bubble groups do, then the coalescence can cause a dryout of the liquid layer under the coalesced bubbles in the bubble groups. Alternatively, it is thought that the coalescence between consecutive bubbles may cause the formation of a vapor column, obstructing the supply of liquid towards the heated wall. In particular, the present visualization shows that the coalescence between adjacent bubbles usually leads to the agglomeration of vapor remnants accompanied by the vaporization of interleaved liquid layer; then, the coalesced bubble separates from the surface in the same way as the discrete bubble. Illustrations based on the present observations are summarized schematically in Fig. 13. Fig. 13(a) and (b) show a typical single bubble departure, and (c) shows the typical coalescence between adjacent bubbles described by Bonjour et al. [16]. The photos of the present work illustrate the coalescence behavior of flow boiling, as shown in Fig. 13(d) through (j). Fig. 13(d) illustrates the coalescence of two neighboring bubbles and then shows that the coalesced bubble does not separate into two stems like (c) but with only one stem (or bubble neck). When two bubbles merge, the vapor remnants below the bubbles are also coalesced and unified with the evaporation of the partial liquid layer. These features can be described by considering the effects of mass flux and subcooling in a pressure condition, as shown in Fig. 13(e) and (f). At higher subcooling and mass flux, bubbles are smaller and drift toward one side of the flow direction. In particular, Fig. 13(f) is also reported in boiling water visualization of Chang et al. [12], who confirmed the existence of the liquid sublayer below coalesced bubbles. Furthermore, external flowing bubbles cause the coalescence

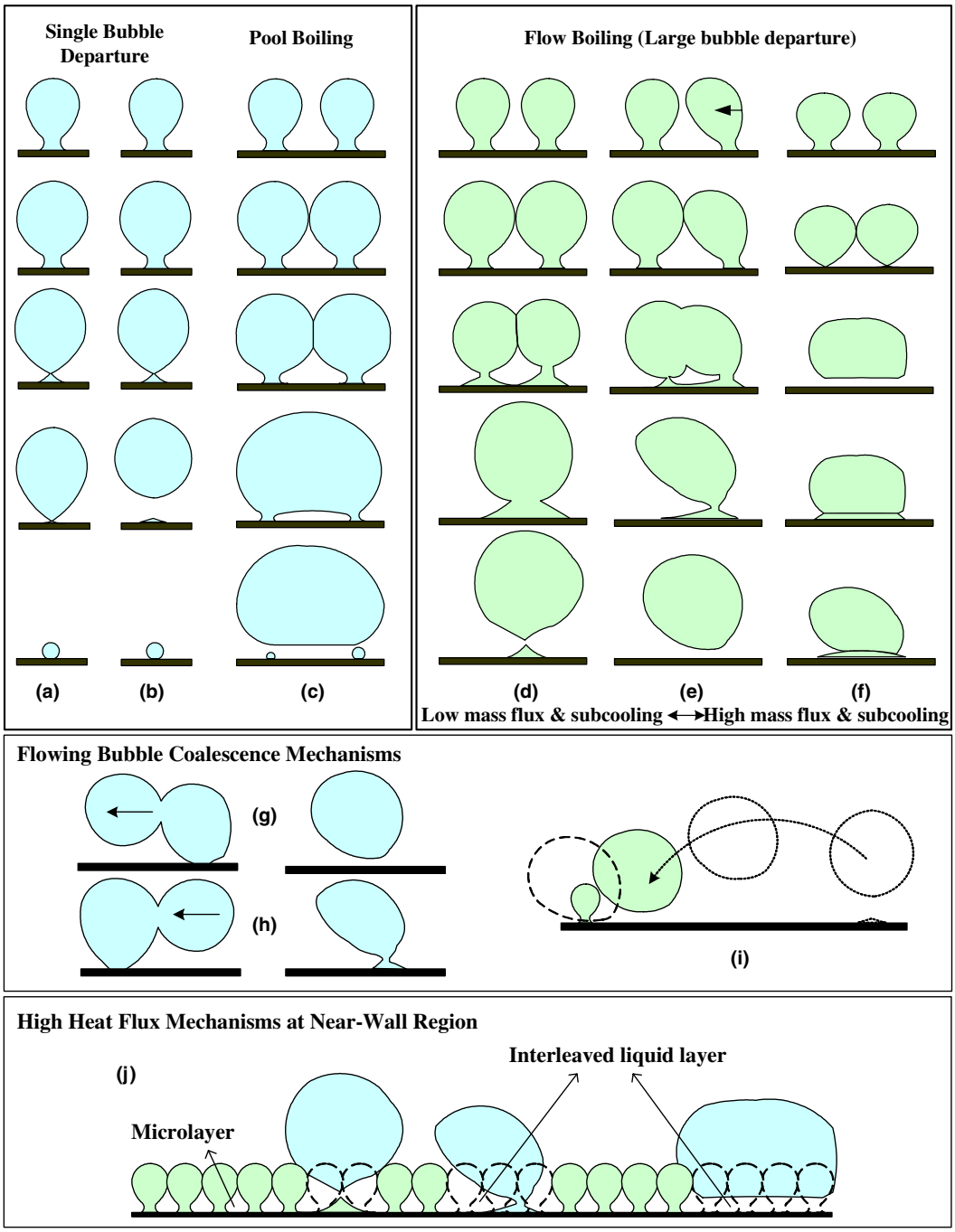

Fig. 13. Coalescence behaviors.

phenomena, as shown in Fig. 13(g) through (i). The flowing bubbles speed up the separation of attached bubbles and form larger, coalesced bubbles. In a high flux with fully developed boiling, the coalescence phenomena are characterized by the three ways shown in Fig. 13(j). The present work provides conclusive, visual evidence that three coalescence modes exist, subject to local thermodynamic conditions, such as mass flow and the subcooling among single discrete bubbles growing from the wall.

4. Conclusions

In the present work, the subcooled flow boiling phenomenon of R-134a, at under 7 and 14.5 bars of pressure, has been successfully observed with the help of recent digital image technology. The visualization is focused on the near-wall region with microstructures in the flow boiling. The visualization results of images, with the spatial resolution of ~10 μm per pixel, lead us to the following conclusions:

(a) R-134a has boiling characteristics similar to those of traditional fluids in subcooled flow boiling.
(b) The characteristic structures of the near-wall region were observed to be as follows:
    1. vapor remnants below the discrete bubble and the coalesced bubble,
    2. coalesced large bubbles and vapor clots at a sufficiently high heat flux,
    3. an interleaved liquid layer between the vapor remnants and bubbles.
(c) The coalesced bubble is detached from the wall as a single bubble detachment, like a bubble neck, because of the agglomeration of vapor remnants.
(d) Three types of coalescence are observed, subject to local thermodynamic conditions, such as mass flow and the subcooling among discrete bubbles growing from the wall.
(e) A bubble layer is divided as follows:
    4. a near-wall bubble layer with small bubbles,
    5. a flowing bubble layer with large coalesced bubbles.
(f) The CHF is the result of the dryout of the near-wall bubble layer below the large vapor clot, which is characterized by coalescence behaviors of vapor remnants and bubbles accompanied by the dryout of the interleaved liquid layer in the near-wall bubble layer.
(g) Further investigation is required for a more reliable distinction between the near-wall bubble layer and the flowing bubble layer.

Acknowledgements

This work was supported by the "*National Laboratory*" program of the Korean Ministry Of Science and Technology(MOST). Special thanks are given to Dr. S.Y. Chun, Dr. S.K. Moon and Mr. S.D. Hong in KAERI.

References

[1] F.C. Gunther, Photographic study of surface-boiling heat transfer to water with forced convection, Trans. ASME 73 (1951) 115–121.
[2] G.J. Kirby, R. Stainforth, J.H. Kinneir, A visual study of forced convection boiling—Part 2. Flow patterns and burnout for a round test section, AEEW-R-506, UKAEA, Winfrith, 1967.
[3] G.P. Celata, M. Cumo, A. Mariani, G. Zummo, A mechanistic model for the prediction of water-subcooled-flow-boiling critical heat flux at high liquid velocity and subcooling, Fusion Technol. 29 (1996) 499–511.
[4] L.S. Tong, A.A. Bishop, L.E. Efferding, A photographic study of subcooled boiling flow and DNB of Freon-113 in a vertical channel, ASME paper 66-WA/HT-3, 1966.
[5] R.J. Mattson, F.G. Hammitt, L.S. Tong, A photographic study of subcooled flow boiling and the boiling crisis in Freon-113, ASME paper, 73-HT-39, 1973.
[6] J.E. Galloway, I. Mudawar, CHF Mechanism in flow boiling from a short heated wall—I, Examination of near-wall conditions with the aid of photomicrography and high-speed video imaging, Int. J. Heat Mass Transfer 36 (1993) 2527–2540.
[7] J.C. Sturgis, I. Mudawar, Critical heat flux in a long, rectangular channel subjected to one-sided heating—I. Flow visualization, Int. J. Heat Mass Transfer 42 (1999) 1835–1847.
[8] J. Weisman, B.S. Pei, Prediction of critical heat flux in flow boiling at low qualities, Int. J. Heat Mass Transfer 26 (1983) 1463–1477.
[9] P.S. Larson, L.S. Tong, Void fraction in subcooled flow boiling, J. Heat Transfer 9 (1969) 471–476.
[10] C.H. Lee, I.A. Mudawar, A mechanistic CHF model for subcooled flow boiling based on local bulk flow conditions, Int. J. Multiphase Flow 14 (1988) 711.
[11] T.H. Chun, W.P. Baek, S.H. Chang, An integral equation model for critical heat flux at subcooled and low quality flow boiling, Nucl. Eng. Des. 199 (2000) 13–29.
[12] S.H. Chang, I.C. Bang, W.P. Baek, A photographic Study on the near-wall bubble behavior in subcooled flow boiling, Int. J. Thermal Sci. 41 (2002) 609–618.
[13] Y. Katto, A physical approach to critical heat flux of subcooled flow boiling in round tubes, Int. J. Heat Mass Transfer 33 (1990) 611–620.
[14] J. Mitrovic, Das abreissen von dampfblasen an festen heizflachen, Int. J. Heat Mass Transfer 26 (1983) 955–963.
[15] H.J. Chung, H.C. No, Simultaneous visualization of dry spots and bubbles for pool boiling of R-113 on a horizontal heater, Int. J. Heat Mass Transfer 46 (2003) 2239–2251.
[16] J. Bonjour, M. Clausse, M. Lallemand, Experimental study of the coalescence phenomenon during nucleate pool boiling, Exp. Thermal Fluid Sci. 20 (2000) 180–187.
[17] ANSI/ASME PTC 19.1, ASME Performance Test Codes: Supplement on Instruments and Apparatus, Part 1: Measurement Uncertainty, 1985.